# Bayesian inference of the critical end point in a (2 + 1)-flavor system from holographic QCD

Liqiang Zhu,[1,*] Xun Chen,[1,2,3,†] Kai Zhou,[4,5,‡] Hanzhong Zhang,[1,§] and Mei Huang[6,‖]

[1]*Key Laboratory of Quark and Lepton Physics (MOE) and Institute of Particle Physics, Central China Normal University, Wuhan 430079, China*

[2]*School of Nuclear Science and Technology, University of South China, Hengyang 421001, China*

[3]*INFN—Istituto Nazionale di Fisica Nucleare—Sezione di Bari, Via Orabona 4, 70125 Bari, Italy*

[4]*School of Science and Engineering, The Chinese University of Hong Kong, Shenzhen (CUHK-Shenzhen), Guangdong, 518172, China*

[5]*Frankfurt Institute for Advanced Studies, Ruth Moufang Strasse 1, D-60438, Frankfurt am Main, Germany*

[6]*School of Nuclear Science and Technology, University of Chinese Academy of Sciences, Beijing 100049, China*

(Received 7 April 2025; accepted 26 June 2025; published 15 July 2025)

We present a Bayesian holographic model constructed by integrating the equation of state and baryon number susceptibility at zero chemical potential from lattice quantum chromodynamics (QCD). The model incorporates error estimates derived from lattice data. With this model, we systematically investigate the thermodynamic properties of the 2 + 1-flavor QCD system. Using Bayesian inference, we perform precise calibration of the model parameters and determined the critical end point (CEP) position under the maximum a posterior (MAP) estimation to be $(T^c, \mu_B^c) = (0.0859\ \text{GeV}, 0.742\ \text{GeV})$. Additionally, we predict the CEP positions within 68% and 95% confidence levels, yielding $(T^c, \mu_B^c)_{68\%} = (0.0820 - 0.0889, 0.71 - 0.77)$ GeV and $(T^c, \mu_B^c)_{95\%} = (0.0816 - 0.0898, 0.71 - 0.79)$ GeV, respectively. Moreover, to validate the reliability and predictive power of our approach, we conduct a comprehensive comparison between our predictions and potential CEP locations proposed by other theoretical models. This work not only establishes a novel Bayesian framework for holographic modeling but also provides valuable insights and theoretical support for exploring phase transitions in strongly interacting matter under extreme conditions.

DOI: 10.1103/wpts-lbtr

## I. INTRODUCTION

In the context of the Standard Model, the strong interaction among quarks and gluons is described by quantum chromodynamics (QCD). A fundamental prediction of QCD based upon its asymptotic properties is that, at sufficiently high temperatures or densities, strongly interacting matter transitions from confined hadronic state into a novel deconfined state called quark-gluon plasma (QGP) [1–6]. In this new state, quarks and gluons are no longer confined within hadrons but instead can interact and move freely. This new state represent the behavior of QCD matter under extreme conditions. The exploration of this transition, and more generally of the QCD phase diagram, has been a longstanding pursuit in high energy physics and remains a central area of inquiry [7–12].

Theoretically, the primary method for investigating the QCD phase diagram relies on first-principle lattice calculations. While the equation of state (EoS) can be reliably obtained at finite temperatures at zero and small chemical potentials, the inherent sign problem in lattice simulations presents obstacles when applying the simulation to situations involving finite baryon density. To gain deeper insights into the QCD phase diagram, a variety of alternative theoretical frameworks have also been employed including the functional renormalization group (FRG) [7,13], the Dyson-Schwinger equations (DSEs) [14–16], and effective QCD models including the random matrix model (RMM) [17], the Nambu-Jona-Lasinio (NJL) models [18–22]. These approaches provide a rich array

*Contact author: zhuliqiang@mails.ccnu.edu.cn
†Contact author: chenxun@usc.edu.cn
‡Contact author: zhoukai@cuhk.edu.cn
§Contact author: zhanghz@mail.ccnu.edu.cn
‖Contact author: huangmei@ucas.ac.cn

*Published by the American Physical Society under the terms of the Creative Commons Attribution 4.0 International license. Further distribution of this work must maintain attribution to the author(s) and the published article's title, journal citation, and DOI. Funded by SCOAP³.*

of theoretical tools and perspectives for understanding the behavior of strongly interacting matter.

In recent decades, the AdS/CFT correspondence [23] has become an increasingly important nonperturbative framework for studying both hadronic physics and hot/dense QCD matter. This theoretical framework not only offers profound insights into hadrons [24–32], but also opens new perspectives for investigating QCD matter under extreme conditions [33–57]. Among the numerous studies conducted under this framework, the Einstein-Maxwell-dilaton (EMD) model [32–34,36–46,49,51,54] has proven particularly effective at capturing key features of QGP. Concurrently, with the advancement of machine learning techniques, these methods have been applied to holography to construct models that utilize specific experimental and lattice QCD data to determine the bulk metric [58–70]. Unlike conventional holographic models, this data-driven approach offers a powerful avenue for advancing our understanding of the properties of QGP.

Bayesian inference has found extensive applications in heavy-ion physics, addressing several critical analysis such as determining jet transport coefficients, modeling energy loss distributions, estimating bulk viscosity and QCD EoS, etc., [71–80]. Additionally, it employs global fitting techniques to estimate parameters from a diverse range of observables [79,81–83]. Recently, in Ref. [84], Bayesian inference was applied to the EMD model, where specific functional forms for the dilaton potential $V(\phi)$ and the coupling between the dilaton and gauge fields $f(\phi)$ were assumed. In this study, we adopt the potential reconstruction method, where one can input either the dilaton or a metric to determine the dilaton potential, and then incorporate Bayesian inference into the EMD model. A significant advantage of the potential reconstruction method in our model is that it enables analytical solutions, thus offering robust theoretical support for subsequent investigation over different interesting physics.

Compared to the machine learning-based EMD model [69,85], a key feature of this work is the systematic incorporation of error bars derived from lattice QCD data, allowing us to provide confidence intervals for the derived physics rather than relying solely on best-fit estimates. This approach enhances the reliability and robustness of our results. The structure of the remainder of this paper is organized as follows: Section. II provides a detailed review of the EMD model, outlining its fundamental principles and application background; Section III delves into our specific procedures of parameter estimation using Bayesian inference, illustrating how the lattice data including their error estimation can be utilized to effectively calibrate our model with more robustness; In Sec. IV, we thoroughly present various thermodynamic quantities derived from our Bayesian calibrated holographic model, including energy density and pressure; Section V focuses on the critical end point (CEP) positions predicted by our model, comparing these findings with those of other theoretical frameworks; Lastly, Sec. VI concludes the paper by summarizing the main results and suggesting directions for future research.

## II. THE REVIEW OF HOLOGRAPHIC EMD MODEL

In this section, we provide a comprehensive review of the five-dimensional EMD system from the perspective of potential reconstruction [36–39,47,49–51,86–89]. The action of the system incorporates a gravitational field $g^s_{\mu\nu}$, a Maxwell field $A_\mu$, and a neutral dilaton scalar field. Within the string frame, its dynamical behavior is characterized by the following equation

$$S_b = \frac{1}{16\pi G_5}\int d^5x\sqrt{-g^s}e^{-2\phi_s} \times\left[R_s - \frac{f_s(\phi_s)}{4}F^2 + 4\partial_\mu\phi_s\partial^\mu\phi_s - V_s(\phi_s)\right], \quad (1)$$

Here, $f(\phi)$ denotes the gauge kinetic function that interacts with the Maxwell field $A_\mu$, while $V(\phi)$ signifies the potential of the dilaton field, and $G_5$ refers to the Newton constant in a five-dimensional spacetime. The specific forms of $f(\phi)$ and $V(\phi)$ can be systematically identified by solving the equations of motion (EoMs). To delve deeper into the thermodynamic characteristics of quantum chromodynamics (QCD), we perform a transformation of the action from the string frame to the Einstein frame based on the following relations,

$$\phi_s = \sqrt{\frac{3}{8}}\phi, \qquad g^s_{\mu\nu} = g_{\mu\nu}e^{\sqrt{\frac{2}{3}}\phi}, \qquad f_s(\phi_s) = f(\phi)e^{\sqrt{\frac{2}{3}}\phi}, \qquad V_s(\phi_s) = e^{-\sqrt{\frac{2}{3}}\phi}V(\phi). \quad (2)$$

After transforming to the Einstein frame, the action takes the following form

$$S_b = \frac{1}{16\pi G_5}\int d^5x\sqrt{-g} \times\left[R - \frac{f(\phi)}{4}F^2 - \frac{1}{2}\partial_\mu\phi\partial^\mu\phi - V(\phi)\right]. \quad (3)$$

The EoMs obtained from the action are listed as follows

$$\begin{aligned} R_{MN} - \frac{1}{2}g_{MN}R - T_{MN} &= 0, \\ \nabla_M\left[f(\phi)F^{MN}\right] &= 0, \\ \partial_M[\sqrt{-g}\partial^M\phi] - \sqrt{-g}\left(\frac{\partial V}{\partial\phi} + \frac{F^2}{4}\frac{\partial f}{\partial\phi}\right) &= 0, \end{aligned} \quad (4)$$

where

$$T_{MN} = \frac{1}{2}\left(\partial_M\phi\partial_N\phi - \frac{1}{2}g_{MN}(\partial\phi)^2 - g_{MN}V(\phi)\right) + \frac{f(\phi)}{2}\left(F_{MP}F_N^P - \frac{1}{4}g_{MN}F^2\right). \tag{5}$$

Here, we propose the following assumed form of the metric

$$ds^2 = \frac{L^2e^{2A(z)}}{z^2}\left[-g(z)dt^2 + \frac{dz^2}{g(z)} + d\vec{x}^2\right]. \tag{6}$$

In this framework, $z$ represents the holographic coordinate in five dimensions, with the radius $L$ of the $AdS_5$ space normalized to one. Utilizing the proposed metric ansatz, we can derive the EoMs and the corresponding constraints for the background fields, as detailed below,

$$\phi'' + \phi'\left(-\frac{3}{z} + \frac{g'}{g} + 3A'\right) - \frac{L^2e^{2A}}{z^2g}\frac{\partial V}{\partial\phi} + \frac{z^2e^{-2A}A_t'^2}{2L^2g}\frac{\partial f}{\partial\phi} = 0, \tag{7}$$

$$A_t'' + A_t'\left(-\frac{1}{z} + \frac{f'}{f} + A'\right) = 0, \tag{8}$$

$$g'' + g'\left(-\frac{3}{z} + 3A'\right) - \frac{e^{-2A}A_t'^2z^2f}{L^2} = 0, \tag{9}$$

$$A'' + \frac{g''}{6g} + A'\left(-\frac{6}{z} + \frac{3g'}{2g}\right) - \frac{1}{z}\left(-\frac{4}{z} + \frac{3g'}{2g}\right) + 3A'^2 + \frac{L^2e^{2A}V}{3z^2g} = 0, \tag{10}$$

$$A'' - A'\left(-\frac{2}{z} + A'\right) + \frac{\phi'^2}{6} = 0. \tag{11}$$

Among these five equations, only four are linearly independent. The horizon ($z = z_h$) is the boundary condition for the equations of motion [Eqs. (7)–(11)], and horizon is also the boundary of the black hole, which physically corresponds to the introduction of temperature, and is represented as follows

$$A_t(z_h) = g(z_h) = 0. \tag{12}$$

As we approach the infrared (IR) boundary at $z \to z_h$, we impose that the metric in the string frame approaches $AdS_5$. The ultraviolet (UV) boundary ($z = 0$) conditions are as follows

$$A(0) = -\sqrt{\frac{1}{6}}\phi(0) = 0, g(0) = 1, A_t(0) = \mu + \rho' z^2 + \cdots. \tag{13}$$

The parameter $\mu$ represents the baryon chemical potential, while $\rho'$ corresponds to a quantity proportional to the baryon number density. The connection between $\mu$ and the quark chemical potential is expressed as $\mu = 3\mu_q$. The procedure for computing the baryon number density is detailed in [43,90]

$$\rho = \left|\lim_{z\to 0}\frac{\partial\mathcal{L}}{\partial(\partial_z A_t)}\right| = -\frac{1}{16\pi G_5}\lim_{z\to 0}\left[\frac{e^{A(z)}}{z}f(\phi)\frac{d}{dz}A_t(z)\right]. \tag{14}$$

In the Einstein frame, the Lagrangian density $\mathcal{L}$ enables the explicit determination of the EoMs using analytical methods

$$\begin{aligned}
\phi'(z) &= \sqrt{-6\left(A'' - A'^2 + \frac{2}{z}A'\right)},\\
A_t(z) &= \sqrt{\frac{-1}{\int_0^{z_h} y^3e^{-3A}dy\int_{y_g}^{y}\frac{x}{e^Af}dx}}\int_{z_h}^{z}\frac{y}{e^Af}dy,\\
g(z) &= 1 - \frac{\int_0^{z} y^3e^{-3A}dy\int_{y_g}^{y}\frac{x}{e^Af}dx}{\int_0^{z_h} y^3e^{-3A}dy\int_{y_g}^{y}\frac{x}{e^Af}dx},\\
V(z) &= -3z^2ge^{-2A}\left[A'' + 3A'^2 + \left(\frac{3g'}{2g} - \frac{6}{z}\right)A' - \frac{1}{z}\left(\frac{3g'}{2g} - \frac{4}{z}\right) + \frac{g''}{6g}\right].
\end{aligned} \tag{15}$$

The parameter $y_g$, as the only undetermined constant, may be linked to the chemical potential $\mu$ in a specific manner. This is accomplished by expanding the field $A_t(z)$ in the vicinity of the boundary at $z = 0$, resulting in

$$A_t(0) = \sqrt{\frac{-1}{\int_0^{z_h} y^3e^{-3A}dy\int_{y_g}^{y}\frac{x}{e^Af}dx}} \times\left(-\int_0^{z_h}\frac{y}{e^Af}dy + \frac{1}{e^{A(0)}f(0)}z^2 + \cdots\right). \tag{16}$$

Following the principles of the anti–de Sitter/conformal field theory (AdS/CFT) correspondence, the chemical potential of the system can be characterized as

$$\mu = -\sqrt{\frac{-1}{\int_0^{z_h} y^3e^{-3A}dy\int_{y_g}^{y}\frac{x}{e^Af}dx}}\int_0^{z_h}\frac{y}{e^Af}dy. \tag{17}$$

The function form of the gauge kinetic term $f(z)$ is specified as [69,85,91]

$$f(z) = e^{cz^2 - A(z) + k}. \tag{18}$$

The function $f(z)$ encapsulates the relationship between the model and the chemical potential, guided by the baryon

number susceptibility. Additionally, this particular choice of $f(z)$ is made to simplify the derivation of the analytical solution. The connection between the integration constant $y_g$ and the chemical potential $\mu$ is given by

$$e^{-cy_g^2} = \frac{\int_0^{z_h} y^3 e^{-3A-cy^2} dy}{\int_0^{z_h} y^3 e^{-3A} dy} - \frac{(1-e^{-cz_h^2})^2}{2c\mu^2 e^k \int_0^{z_h} y^3 e^{-3A} dy}. \tag{19}$$

From this, we are able to derive

$$\begin{aligned} g(z) &= 1 - \frac{1}{\int_0^{zh} dx x^3 e^{-3A(x)}} \left[ \int_0^z dx x^3 e^{-3A(x)} + \frac{2c\mu^2 e^k}{(1-e^{-cz_h^2})^2} \det \mathcal{G} \right], \\ \phi'(z) &= \sqrt{6(A'^2 - A'' - 2A'/z)}, \\ A_t(z) &= \mu \frac{e^{-cz^2} - e^{-cz_h^2}}{1 - e^{-cz_h^2}}, \\ V(z) &= -\frac{3z^2 g e^{-2A}}{L^2} \left[ A'' + A' \left( 3A' - \frac{6}{z} + \frac{3g'}{2g} \right) - \frac{1}{z} \left( -\frac{4}{z} + \frac{3g'}{2g} \right) + \frac{g''}{6g} \right], \end{aligned} \tag{20}$$

where

$$\det \mathcal{G} = \begin{vmatrix} \int_0^{z_h} dy y^3 e^{-3A(y)} & \int_0^{z_h} dy y^3 e^{-3A(y)-cy^2} \\ \int_{z_h}^{z} dy y^3 e^{-3A(y)} & \int_{z_h}^{z} dy y^3 e^{-3A(y)-cy^2} \end{vmatrix}. \tag{21}$$

The Hawking temperature [92] and entropy corresponding to this black hole solution can be represented as follows

$$\begin{aligned} T &= \frac{|g'(z)|}{4\pi} \\ &= \frac{z_h^3 e^{-3A(z_h)}}{4\pi \int_0^{z_h} dy y^3 e^{-3A(y)}} \left[ 1 + \frac{2c\mu^2 e^k \left( e^{-cz_h^2} \int_0^{z_h} dy y^3 e^{-3A(y)} - \int_0^{z_h} dy y^3 e^{-3A(y)} e^{-cy^2} \right)}{(1-e^{-cz_h^2})^2} \right], \end{aligned} \tag{22}$$

$$S = \frac{e^{3A(z_h)}}{4G_5 z_h^3}. \tag{23}$$

In order to solve the system analytically, we make the following ansatz

$$A(z) = d * \ln(az^2 + 1) + d * \ln(bz^4 + 1). \tag{24}$$

The function $A(z)$ is designed to reproduce the proper entropy behavior and impose constraints on the temperature-dependent model inspired by Refs. [38,49,69,85]. Within the string frame, $A_s(z)$ is expressed as

$$A_s(z) = A(z) + \sqrt{\frac{1}{6}} \phi(z). \tag{25}$$

The model involves five undetermined parameters, which can be fixed using Bayesian inference based on the equation of state (EoS) data provided by lattice calculations. Additionally, a parameter $c$ can be concurrently identified through the analysis of baryon number susceptibility. Once the entropy is obtained, the free energy can then be derived as

$$\begin{aligned} F &= -\int s dT - \int \rho d\mu \\ &= -\int s \left( \frac{\partial T}{\partial z_h} dz_h + \frac{\partial T}{\partial \mu} d\mu \right) - \int \rho d\mu \\ &= \int_{z_h}^{\infty} s \frac{\partial T}{\partial z_h} dz_h - \int_0^{\mu} \left( \frac{\partial T}{\partial \mu} d\mu + \rho \right) d\mu. \end{aligned} \tag{26}$$

The free energy has been normalized such that it approaches zero as $z_h \to \infty$. Consequently, The energy density associated with the system can be formulated as

$$\epsilon = -p + sT + \mu\rho. \tag{27}$$

In conditions with a nonzero chemical potential, the squared sound speed can be determined using the approaches outlined in [93–95]

$$C_s^2 = \frac{s}{T\left(\frac{\partial s}{\partial T}\right)_\mu + \mu\left(\frac{\partial \rho}{\partial T}\right)_\mu}. \tag{28}$$

Specific heat capacity refers to the amount of heat absorbed or released by a unit mass of a substance during temperature changes, which can be defined as

$$C_V = T\frac{\partial s}{\partial T}. \tag{29}$$

In this work, we define the scaled second-order baryon number susceptibility as

$$\chi_2^B = \frac{1}{T^2}\frac{\partial \rho}{\partial \mu}. \tag{30}$$

## III. BAYESIAN INFERENCE OF MODEL PARAMETERS

Bayesian inference has proven highly successful in constraining model parameters within relativistic heavy-ion collisions [81,96,97]. Notable applications include determinations of the shear viscosity over entropy density ratio $(\eta/s)$ of the QGP medium [82,98], the jet transport coefficient $\hat{q}$ [71,99,100], the QCD equation of state [101], nucleon distributions in the nucleus [80], and the analysis of the jet energy loss [72,73,76]. In this work, we leverage Bayesian methods to systematically investigate how lattice QCD results [102,103] constrain the parameter space of the EMD model. Specifically, we infer the posterior distributions of the EMD model parameters $\boldsymbol{\theta}(a, b, c, d, k, G_5)$ to study their influence on predictions for the thermodynamic behaviors of the entropy $S_{\mathrm{BH}}$, baryon susceptibility $\chi_2^B$ and speed of sound squared $C_s^2$. This section outlines the Bayesian inference framework applied to the EMD model, with a schematic of the workflow provided in Fig. 1. Subsection A details the model inputs of the EMD model, including parameter design, selection criteria, as well as their prior distribution. Subsection B describes the model outputs generated from these inputs and the postprocessing steps applied to enable comparison with lattice provided observables. Subsection C elaborates on the technical implementation of the Gaussian process emulator, which bridges the parameter spaces to observables. Finally, subsection D presents specific process of parameter inference, covering the construction of prior distributions, likelihood functions, and posterior distributions, as well as the Markov chain Monte Carlo (MCMC) [104,105] sampling to explore the posterior distribution.

### A. Parameter design

This subsection outlines the design of the EMD model parameters $\boldsymbol{\theta} = (a, b, c, d, k, G_5)$. The process comprises two essential steps: initially, defining the number of design points and their respective value ranges for each parameter; subsequently, strategically distributing these design points within the parameter space.

First, the number of design points, which corresponds to how many sets of parameters $\boldsymbol{\theta} = (a, b, c, d, k, G_5)$ to select in preparing a training dataset for latter emulator construction, should be carefully chosen to balance the computational efficiency against statistical robustness, with the aim to minimize computational expense while ensuring sufficient coverage of the parameter space and accuracy in Bayesian posterior estimation. For this purpose, we select $d$ design points, which are structured into a $d \times 6$ design matrix $\boldsymbol{\Theta} = (\boldsymbol{\theta}_1, \boldsymbol{\theta}_2, \ldots, \boldsymbol{\theta}_d)$, where each row corresponds to a unique parameter set. The allowable range for each parameter is defined to be physically broad enough to

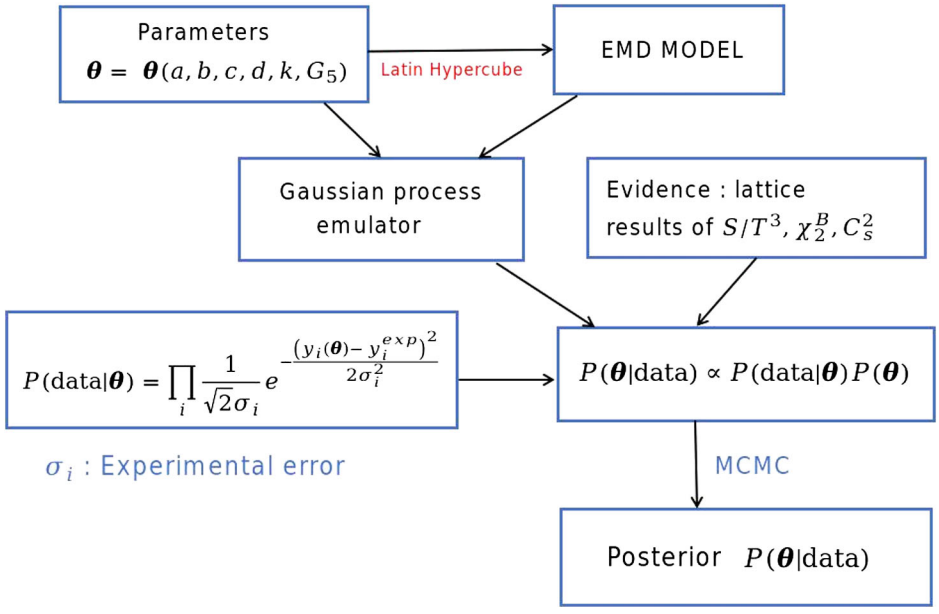



FIG. 1. Overview of the Bayesian parameter inference process.

encompass all plausible configurations while avoiding artificial truncation that could bias the inference.

Next, we employ Latin hypercube sampling (LHS) [106,107] to distribute the design points uniformly across the 6-dimensional parameter space. LHS is a space-filling statistical method optimized for generating representative samples in high-dimensional parameter spaces. Unlike traditional random sampling, LHS partitions each parameter's range into $d$ equal subintervals and draws one sample per subinterval, encuring uniform marginal coverage across all dimensions. The advantage of this stratified sampling method is that it ensures a more uniform distribution of data points, avoiding clustering or missing certain areas. Even with limited computational resources and fewer sample points, it can efficiently cover the entire parameter space. This characteristic is particularly suitable for subsequent modeling (such as emulators like Gaussian processes), where uniformly distributed data can enable more accurate interpolation by the model in high-dimensional parameter spaces, thereby improving the precision of Bayesian inference.

For the 6-dimensional parameter space of the EMD model $[\boldsymbol{\theta} = (a, b, c, d, k, G_5)]$ specifically, we implemented LHS to generate 300 design points, organized into a $300 \times 6$ design matrix $\boldsymbol{\Theta} = (\boldsymbol{\theta_1}, \boldsymbol{\theta_2}, \ldots, \boldsymbol{\theta_{300}})$. While prior studies [108] suggest that ~10 design points typically suffice for acceptable computational accuracy, we prioritized enhanced emulator performance by selecting 300 points—a balance between computational feasibility and statistical fidelity. Each parameter set $\theta_i$ was propagated through the EMD model to compute the corresponding observables $S_{\mathrm{BH}}$, $\chi_2^B$ and $C_s^2$. The resulting 300 output sets were postprocessed (see next subsection) to enable comparison with lattice QCD constraints.

### B. Postprocessing model output

Taking as input with the sampled parameter sets $\boldsymbol{\Theta} = (\boldsymbol{\theta}_1, \boldsymbol{\theta}_2, \ldots, \boldsymbol{\theta}_{300})$, the EMD model generates 300 output vectors $\mathbf{y} = (y_1, y_2, \ldots, y_m)$, where $m$ corresponds to the number of temperature-dependent data points for the lattice observables $S_{\mathrm{BH}}$ (55 points), $\chi_2^B$ (19 points) and $C_s^2$ (55 points) as defined in Eqs. (23), (30), and (28). While constructing independent Gaussian process (GP) emulators for each output variable (see next subsection) is straightforward, direct usage of these outputs in doing so scales poorly with $m$ and neglects inter-output correlations. To address these limitations, we postprocess them by applying principal component analysis (PCA) [109], which reduces the output dimensionality and decorrelate the data while preserving covariant structure.

PCA projects correlated high-dimensionally data into a lower-dimensional subspace spanned by orthogonal principal components (PCs) ordered by their explained variance. For our case, the outputs are organized into a $300 \times m$ matrix $Y$, where rows represent design points and columns correspond to observables at discrete temperatures. Prior to PCA, $Y$ is standardized by centering each column (subtracting the mean) and scaling to unit variance, ensuring equal weighting across temperature points.

The standardized data is decomposed via singular value decomposition (SVD) to obtain the orthonormal transformation matrix $V$, whose columns $v_j$ define the PC directions. The projected data in PC space is given by $Z = YV$, where $Z$ is a $300 \times m$ matrix. Each row of $Z$ corresponds to a design point, while columns represent PCs ranked by descending variance contribution, The first PC captures the dominant covariance pattern in $Y$, with subsequent PCs encoding orthogonal modes of decreasing significance.

For correlated physical observables, the leading PCs typically encapsulate the majority of system variance. Figure 2 illustrates the cumulative explained variance versus the number of PCs retained for $S_{\mathrm{BH}}$, $\chi_2^B$ and $C_s^2$. While 99% of the variance is captured by the first three PCs across all observables, we conservatively retain the 6 PCs to ensure robust emulation of subtle features. This reduces the effective dimensionality from $m = 55$, 19, 55 to 6, drastically lowing computational costs without sacrificing predictive accuracy.

The PCA workflow was implemented using the scikit-learn library in Python, leveraging its optimized numerical

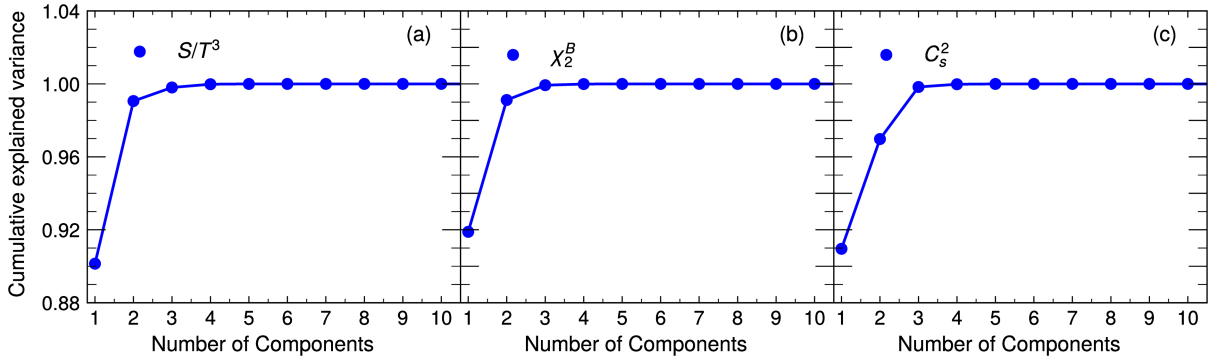



FIG. 2. Cumulative explained variance versus principal component (PC) count for (a) $S_{\mathrm{BH}}$, (b) $\chi_2^B$ and (c) $C_s^2$. The first 3 PCs capture 99% of the variance in all cases, while the first 6 PCs are retained for conservative emulation.

routines for efficient SVD computation and component projection. The retained PCs, $z_1, z_2, \ldots, z_6$, serve as uncorrelated targets for subsequent Gaussian process emulation, enabling efficient Bayesian inference while preserving interobservable correlations.

### C. Gaussian processes emulator

To reduce computational costs while preserving predictive accuracy later in the extensive Bayesian exploration for the posterior distribution, we employ a Gaussian process (GP) emulator [110] as a surrogate model for the full EMD model calculation. A GP is a probabilistic model defines a distribution over functions where any finite set of function evaluations follows a multivariate Gaussian distribution. Formally, for input parameters $\boldsymbol{\theta} \in \mathcal{R}^6$ [with design matrix $\boldsymbol{\Theta} = (\boldsymbol{\theta}_1, \boldsymbol{\theta}_2, \ldots, \boldsymbol{\theta}_{300})$] and outputs $\mathbf{Y} = (\mathbf{y}_1, \mathbf{y}_2, \ldots, \mathbf{y}_{300})$, the GP is fully specified by: (1) a mean function $\mu(\boldsymbol{\theta})$: Typically set to zero after centering the data [$Y \leftarrow Y - \text{mean}(Y)$], simplifying prior assumptions; and (2) a covariance kernel $\sigma(\boldsymbol{\theta}, \boldsymbol{\theta}')$: Encodes correlations between outputs at different input points. With these two functions, the Gaussian process provides a flexible framework for modeling complex dependencies and uncertainty in data.

The squared-exponential kernel is adopted for its smoothness and interpretability

$$\sigma(\boldsymbol{\theta}, \boldsymbol{\theta}') = \exp\left(-\frac{|\boldsymbol{\theta} - \boldsymbol{\theta}'|^2}{2\ell^2}\right), \tag{31}$$

where $l > 0$ is the characteristic length scale governing correlation decay rate between input points: Nearby points ($||\boldsymbol{\theta} - \boldsymbol{\theta}'|| \ll l$) are strongly correlated, while distant points ($||\boldsymbol{\theta} - \boldsymbol{\theta}'|| \gg l$) become independent.

For $n = 300$ training points, the outputs $Y$ jointly follow a multivariate normal distribution

$$\mathbf{Y} \sim \mathcal{N}(\mathbf{0}, \mathbf{K}),$$
$$\mathbf{K} = \begin{pmatrix} \sigma(\boldsymbol{\theta}_1, \boldsymbol{\theta}_1) & \sigma(\boldsymbol{\theta}_1, \boldsymbol{\theta}_2) & \cdots & \sigma(\boldsymbol{\theta}_1, \boldsymbol{\theta}_{300}) \\ \vdots & \vdots & \ddots & \vdots \\ \sigma(\boldsymbol{\theta}_{300}, \boldsymbol{\theta}_1) & \sigma(\boldsymbol{\theta}_{300}, \boldsymbol{\theta}_2) & \cdots & \sigma(\boldsymbol{\theta}_{300}, \boldsymbol{\theta}_{300}) \end{pmatrix}, \tag{32}$$

where $K$ is the $300 \times 300$ covariance matrix.

Then, when given test inputs $\boldsymbol{\Theta}_*$, GP predict the distribution for its outputs $\mathbf{Y}_*$ is Gaussian as follows:

$$\mathbf{Y}_* | \boldsymbol{\Theta}_*, \boldsymbol{\Theta}, \mathbf{Y} \sim \mathcal{N}(\boldsymbol{\mu}_*, \boldsymbol{\Sigma}*), \tag{33}$$

$$\boldsymbol{\mu}_* = \mathbf{K} * \mathbf{K}^{-1}\mathbf{Y}, \tag{34}$$

$$\boldsymbol{\Sigma}* = \mathbf{K} * * - \mathbf{K}_* \mathbf{K}^{-1} \mathbf{K}_*^{\mathrm{T}}, \tag{35}$$

where $\mathbf{K}_* = \sigma(\boldsymbol{\Theta}_*, \boldsymbol{\Theta})$ and $\mathbf{K}_{**} = \sigma(\boldsymbol{\Theta}_*, \boldsymbol{\Theta}_*)$.

The EMD model is treated as a latent function $f(\boldsymbol{\theta})$ with input $\boldsymbol{\theta} = (a, b, c, d, k, G_5)$, where $f$ maps them to observables (more specifically, the first 6 principle components of) $S_{\mathrm{BH}}$, $\chi_2^B$, and $C_s^2$. The GP emulator training proceeds as follows: (1) center outputs $Y$ by subtracting the empirical mean; (2) maximize the marginal likelihood to determine $l$ for the kernel; (3) use Eqs. (33)–(35) to predict $Y_*$ at new $\boldsymbol{\Theta}_*$.

This framework enables efficient interpolation across the 6D parameter space while quantifying predictive uncertainty–critical for Bayesian parameter inference.

### D. Bayesian extraction of the model parameters

We are now able to calibrate our EMD model with lattice data (also called evidence in Bayesian inference), specifically, to derive numerical evaluations of the model parameters while simultaneously evaluating their uncertainties. This is essentially an inverse problem, the primary objective of which is to infer unknown model input parameters or physical factors using the available output data [111–114]. Within the Bayesian inference framework, the estimation of model parameters is derived from their posterior distribution, which combines prior information with the likelihood function constructed from observational data to deliver more reliable parameter estimation results,

$$P(\boldsymbol{\theta}|data) \propto P(data|\boldsymbol{\theta})P(\boldsymbol{\theta}) \tag{36}$$

In this context, $\boldsymbol{\theta}$ represents the parameters of the model, while data encompasses the evidence we choose from lattice simulation. This relationship, known as Bayes' theorem, expresses the posterior distribution on the left-hand side, which describes the probability distribution of the parameters conditioned on the observed data. On the right-hand side, $P(data|\boldsymbol{\theta})$ denotes the likelihood function, indicating the chance that the chosen evidence (data) to be observed under particular parameter values. Meanwhile, $P(\boldsymbol{\theta})$ corresponds to the prior distribution, which encapsulates our initial beliefs or assumptions about the parameters before incorporating the observed data.

In the following, we will elaborate on the definitions of the prior distribution and likelihood function, as well as how to efficiently sample from the posterior distribution using the MCMC method.

First, the prior distribution $P(\boldsymbol{\theta})$ captures initial assumptions about the parameters before observing any data. When no specific knowledge is available, a uniform prior is a widely used option, assigning a constant value to $P(\boldsymbol{\theta})$. In this work, each parameter is assumed to be uniformly distributed within a limited design range, thus the Gaussian process emulator's predictions are valid only within these bounds. Accordingly, the prior can be defined as a constant within the design region and zero elsewhere, providing both a practical constraint and a streamlined representation of prior knowledge.

TABLE I. Parameter ranges for prior distribution in the EMD model. Min indicating the minimum value of the parameter, and Max indicating the maximum value of the parameter.

| | Prior | |
|---|---|---|
| Parameter | Min | Max |
| $a$ | 0.110 | 0.310 |
| $b$ | 0.005 | 0.031 |
| $c$ | −0.280 | −0.205 |
| $d$ | −0.240 | −0.110 |
| $k$ | −0.910 | −0.770 |
| $G_5$ | 0.375 | 0.430 |

$$P(\boldsymbol{\theta}) \propto \begin{cases} 1 & \text{if } \min(\boldsymbol{\theta}_i) \le \boldsymbol{\theta}_i \le \max(\boldsymbol{\theta}_i) \quad \text{for all } i, \\ 0 & \text{else.} \end{cases} \tag{37}$$

Setting the prior to zero outside the design region is a strict and cautious assumption, effectively ruling out any possibility of the true parameter values lying beyond the defined limits. However, this rigidity risks overlooking valid parameter spaces, potentially undermining the model's flexibility and predictive power. A more sensible approach is to define broader design ranges, which allow for greater uncertainty in parameter estimation. This ensures the model remains versatile and captures a wider spectrum of plausible parameter values, enhancing both its robustness and practical relevance.

In our study, the prior ranges for the model parameters $\boldsymbol{\theta}(a, b, c, d, k, G_5)$ are comprehensively listed in Table I. By applying these prior ranges to the EMD model, we derived theoretical predictions for $S_{\mathrm{BH}}$, $\chi_2^B$, and $C_s^2$, which are visually presented in Fig. 3.

Next, the likelihood function of the parameters given the observed data, denoted as $P(data|\boldsymbol{\theta})$, quantifies the probability of observing specific data under the model with a given parameter $\boldsymbol{\theta}$, which due to the central limit theorem can be expressed as Gaussian form with the chi-square as the exponent

$$P(data|\boldsymbol{\theta}) = \prod_i \frac{1}{\sqrt{2\pi}\sigma_i} e^{-\frac{[y_i(\boldsymbol{\theta}) - y_i^{\mathrm{lattice}}]^2}{2\sigma_i^2}} \tag{38}$$

where $y_i(\boldsymbol{\theta})$ and $y_i^{\mathrm{lattice}}$ denote our GP emulator predicted observables (specifically, the first 6 PCs) and those from lattice simulation. Note that here $y_i^{\mathrm{lattice}}$ is obtained by applying the same transformation matrix $V$ derived from the PCA as specified in subsection B on the lattice simulated $S_{\mathrm{BH}}$, $\chi_2^B$, and $C_s^2$. In our calculations, the error bars are self-consistently incorporated into the posterior computation within the Bayesian inference framework, specifically reflected in the $\sigma^2$ of the exponential part of our likelihood [Eq. (38)]. The error $\sigma$ includes the error from the lattice data and the error from the Gaussian process emulator, $\sigma^2 = \sigma^2_{\mathrm{lattice}} + \sigma^2_{\mathrm{Gaussian\ emulator}}$.

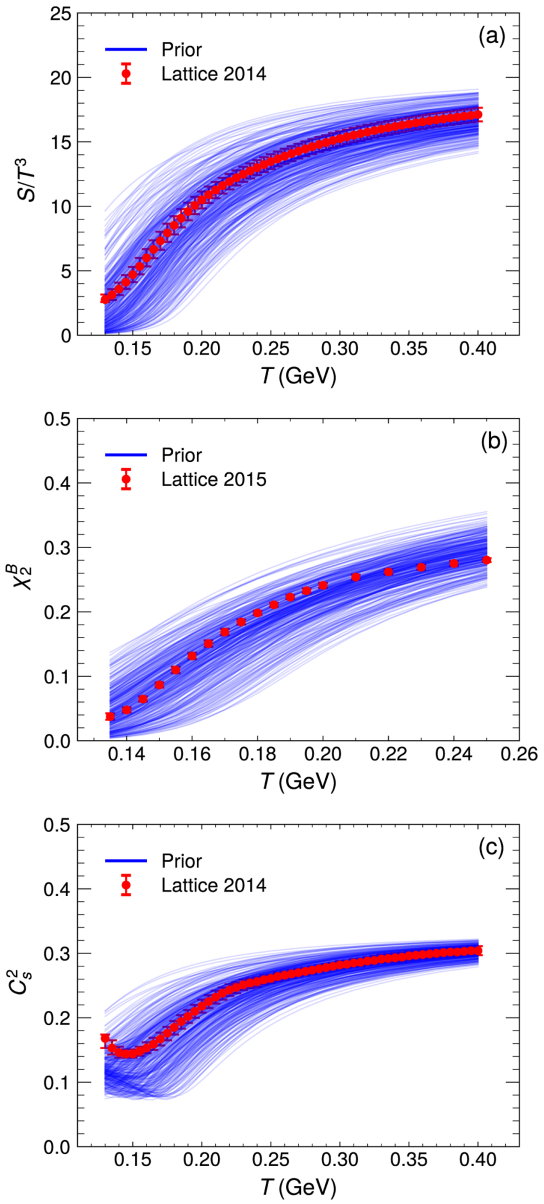



FIG. 3. (a) The prior distribution of entropy as a function of temperature. (b) The prior distribution of baryon number susceptibility as a function of temperature. (c) The prior distribution of the square of the speed of sound as a function of temperature. The lattice results from Refs. [102,103].

In our calculation, we first compute independent likelihood functions for $S_{\mathrm{BH}}$, $\chi_2^B$, and $C_s^2$, then construct a joint likelihood function as the product of individual likelihoods

$$P(data|\boldsymbol{\theta}) = P(data_{S_{\mathrm{BH}}}|\boldsymbol{\theta}) P(data_{\chi_2^B}|\boldsymbol{\theta}) P(data_{C_s^2}|\boldsymbol{\theta}). \tag{39}$$

This multiplicative approach systematically integrates constraints from all observables, ensuring a holistic assessment of parameter compatibility.

Finally, to sample the posterior distribution $P(\boldsymbol{\theta}|data)$, we employ the Metropolis-Hastings algorithm [115,116],

a straightforward and commonly used MCMC sampling technique in Bayesian inference for handling high-dimensional parameter spaces and complex distributions. It iteratively samples by randomly proposing a candidate $\boldsymbol{\theta}'$ from the current position $\boldsymbol{\theta}_i$, determining acceptance based on their posterior probabilities. If accepted, the next position is updated to $\boldsymbol{\theta}_{(i+1)} = \boldsymbol{\theta}'$; otherwise, it remains at $\boldsymbol{\theta}_{(i+1)} = \boldsymbol{\theta}_{(i)}$. Repeating this process produces a sequence $\{\boldsymbol{\theta}_{(1)}, \boldsymbol{\theta}_{(2)}, \ldots, \boldsymbol{\theta}_{(n)}\}$ that eventually converges to the target posterior distribution. After discarding initial "burn-in" samples (typically 10%–20% of the chain) to mitigate transient correlation effects from starting values of the parameters, the remaining chain approximates the target posterior.

To ensure better numerical stability and efficiency for high-dimensional probability calculations, we work with the log-posterior

$$\log P(\boldsymbol{\theta}|data) = \log P(data|\boldsymbol{\theta}) + \log P(\boldsymbol{\theta}) + \text{const} \quad (40)$$

where additive constants after taking logarithm of the distribution are irrelevant for MCMC, which depends only on probability ratios. Thus, terms associated with those additive constants can be disregarded. Specifically, the logarithmic expressions for the prior Eq. (37) and the uniform likelihood Eq. (39) are as follows:

$$\log P(\boldsymbol{\theta}) \propto \begin{cases} 0 & \text{if } \min(\boldsymbol{\theta}_i) \le \boldsymbol{\theta}_i \le \max(\boldsymbol{\theta}_i) \quad \text{for all } i, \\ -\infty & \text{else.} \end{cases} \quad (41)$$

$$\log P(data|\boldsymbol{\theta}) = -\frac{1}{2}\mathbf{y}^T\Sigma^{-1}\mathbf{y} - \frac{1}{2}\log|\Sigma| - \frac{1}{2}\log 2\pi, \quad \mathbf{y} = y(\boldsymbol{\theta}) - y^{\text{lattice}}. \quad (42)$$

The initial "burn-in" phase allows the chain to transition from arbitrary starting points to regions of high posterior density. The required burn-in length depends on the posterior's complexity and the proposal distribution's efficiency. In practice, we employed 120 walkers, which were randomly initialized within the parameter space. An initial 10000 steps were run as a burn-in phase to ensure that the chain adequately converged to the target posterior distribution. After the burn-in phase, an additional 10000 steps were conducted to generate posterior samples. This sample size is sufficient for constructing smooth histogram visualizations; however, it may be excessive for tasks such as calculating medians or other summary statistics. It is worth emphasizing that the total number of samples is determined by the product of the number of walkers and the number of steps.

Once the MCMC sampling is completed, the marginal distributions for each parameter within $\boldsymbol{\theta} = (a, b, c, d, k, G_5)$ can be derived. A marginal distribution is obtained from the posterior distribution by isolating a specific parameter or a group of parameters of interest, while integrating out the remaining parameters. For example, in our model, the marginal distribution of parameter $d$ can be determined by eliminating the contributions of all other parameters through integration.

$$P(d|data) = \int dadbdcdkdG_5 P(\boldsymbol{\theta}|data). \quad (43)$$

For the joint distribution of two parameters, such as $a$ and $d$, it can be calculated as

$$P(a, d|data) = \int dbdcdkdG_5 P(\boldsymbol{\theta}|data). \quad (44)$$

With the evidence (data) chosen as $S/T^3, \chi_2^B$ and $C_s^2$ from the lattice QCD [102,103] into our Bayesian analysis, we add $C_s^2$ to better highlight the phase transition region. Table II summarizes our inferred parameter constraints, reporting the 95% credible intervals and maximum *a posteriori* (MAP) estimates derived from the MCMC. Figure 4 visualizes the posterior distributions using a corner plot (or triangle plot), a standard tool in Bayesian analysis for high-dimensional parameter spaces. It consists of a diagonal subplots and off-diagonal subplots. The diagonal subplots show the marginal distributions of individual parameters, i.e., the marginal probability density of each parameter after integrating out other parameters, and we took the 95% confidence levels and identified the maximum posterior value. The off-diagonal subplots display the joint distributions between pairs of parameters, visualized as 2D density estimates, revealing correlations or degeneracies between parameters, such as trade-offs in how combinations of different parameters accommodate observational constraints. It is evident that the used data from lattice can well calibrate each parameter in our model with clear peak structure, and certain correlations between several parameters like $b$ and $d$ are also shown.

TABLE II. Parameter estimates with posterior 95% confidence levels and MAP values for parameters of the EMD model. Min indicating the minimum value of the parameter, and Max indicating the maximum value of the parameter.

| | Posterior 95% CL | | |
|---|---|---|---|
| Parameter | Min | Max | MAP |
| $a$ | 0.229 | 0.282 | 0.252 |
| $b$ | 0.019 | 0.027 | 0.023 |
| $c$ | −0.261 | −0.231 | −0.245 |
| $d$ | −0.143 | −0.127 | −0.135 |
| $k$ | −0.871 | −0.808 | −0.843 |
| $G_5$ | 0.388 | 0.406 | 0.397 |

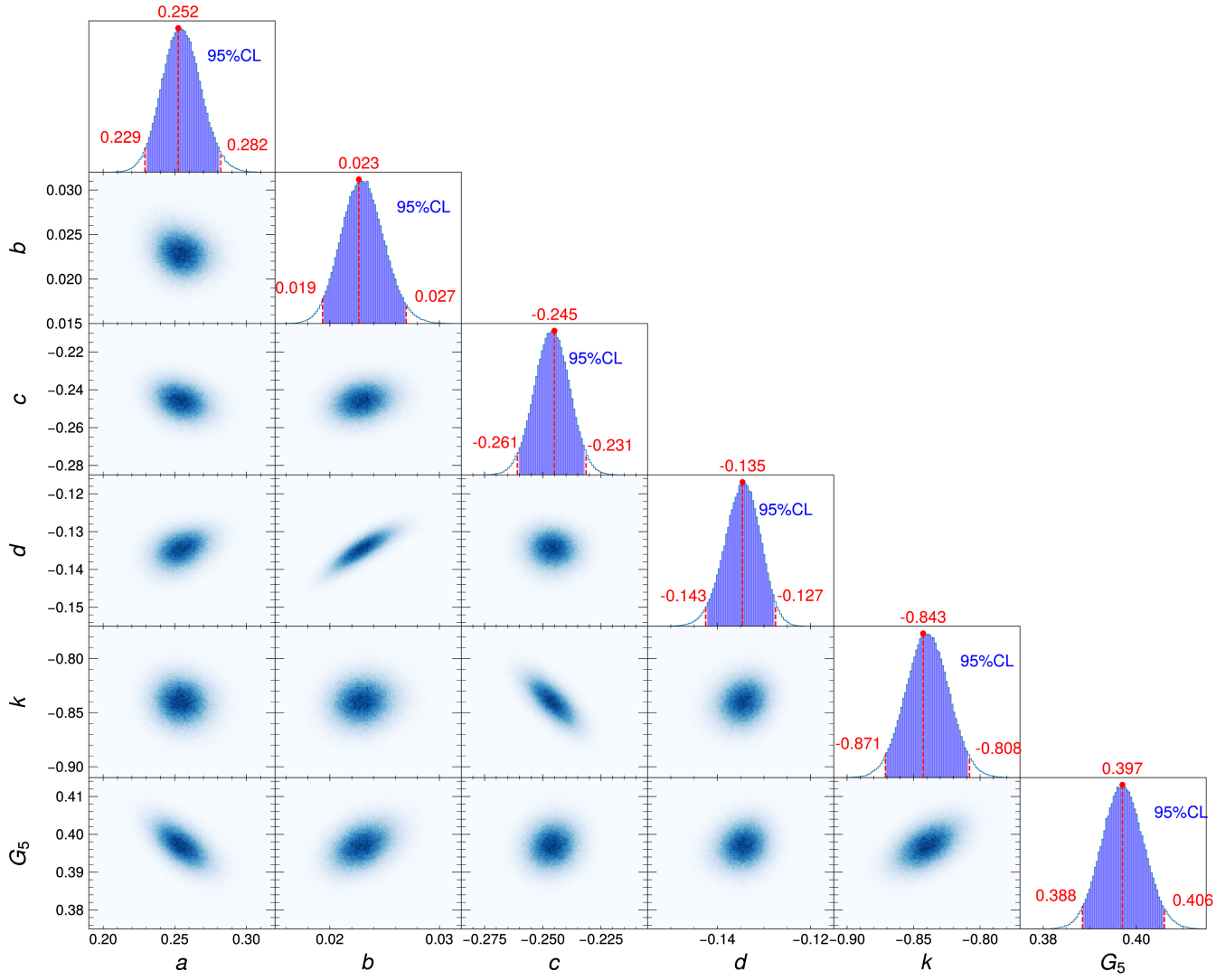



FIG. 4. Diagonal: the marginal posterior distributions of the model parameters, along with the MAP values and the 95% confidence levels for each parameter. Lower triangle: the joint distribution between each pair of parameters.

## IV. THERMODYNAMICS IN THE BAYESIAN HOLOGRAPHIC QCD MODEL

This section systematically evaluates the thermodynamic predictions of our Bayesian-calibrated holographic model. We first analyze the impact of evidence selection by comparing results from two cases in subsection A: (1), case 1: with $S/T^3$ and $\chi_2^B$ as evidence; and (2) case 2: with $S/T^3$, $\chi_2^B$ and $C_s^2$ jointly as evidence. Subsequently, in subsection B we confront our results from case 2 against lattice QCD [102,103], the hadron resonance gas (HRG) model [117], and the hard thermal loop (HTL) model [118].

### A. Evidence selection and thermodynamic consistency

By applying the same Bayesian inference procedures as described above, but with two different cases for evidence, we evaluated the corresponding MAP values for the model parameters, and further derive the thermodynamics by incorporating the EMD model on these parameters constraints.

Key thermodynamic observables using MAP values from case 1 (green curves) and case 2 (blue curves) are displayed in Fig. 5. We see that our model within case 2 yield better agreement with lattice data compared to case 1. Specifically, for entropy ($S/T^3$) and baryon susceptibility ($\chi_2^B$), both cases align with lattice data at $T > 150$ MeV, but case 2 results better captures the inflection near $T \sim 140$ MeV, where $\chi_2^B$ transitions toward the HRG limit [Figs. 5(a)–(b)]. For the square of the speed of sound squared ($C_s^2$), while case 1 underestimates the lattice result in the region $T \sim 150$ MeV, case 2 results resolves the minimum region much better [Fig. 5(f)], reproducing the

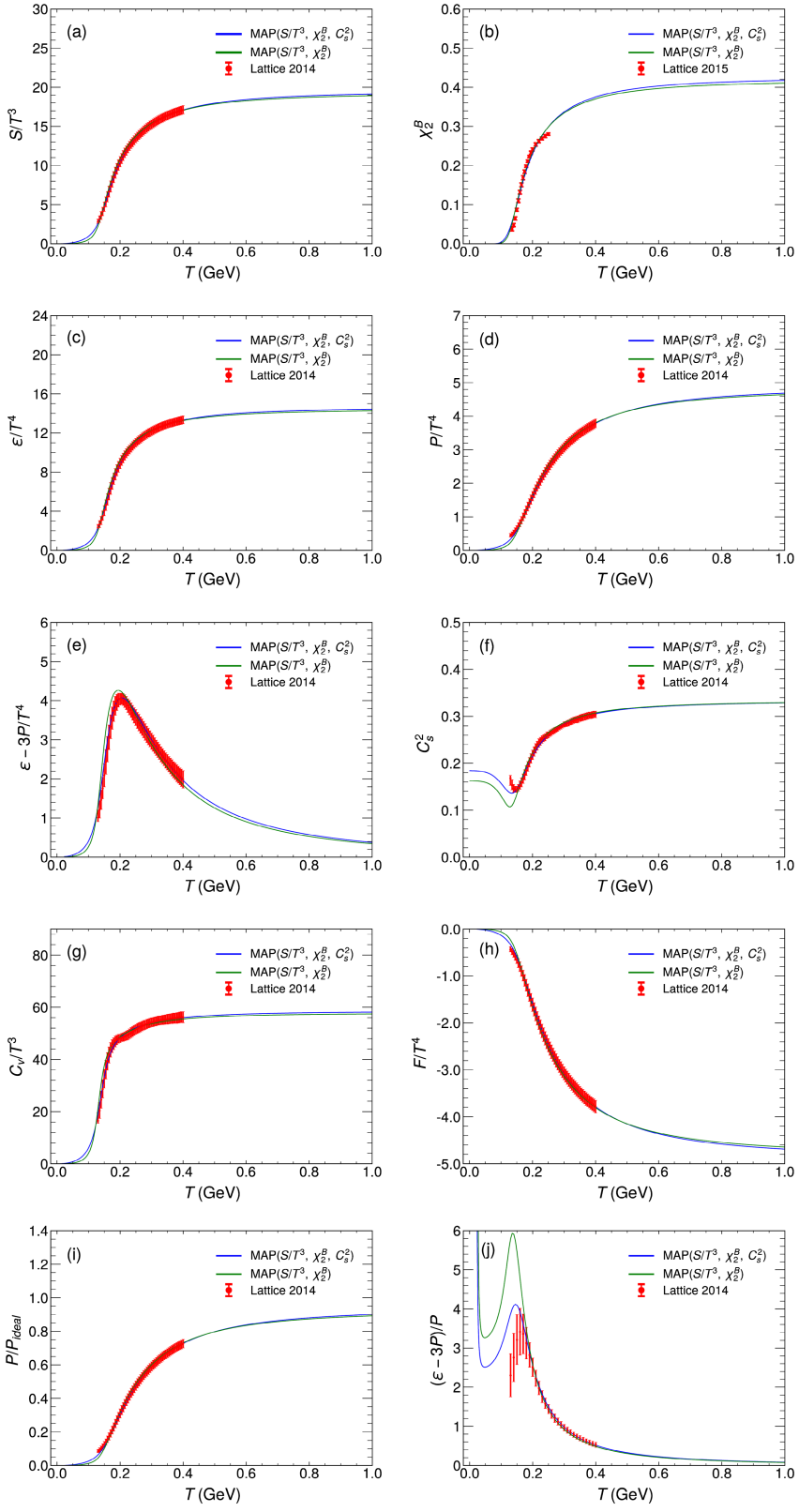



FIG. 5. Using Bayesian inference to compare the posterior thermodynamic results under case 1 and case 2, the label MAP($S/T^3, \chi_2^B$) represents case 1 (with $S/T^3$ and $\chi_2^B$ as evidence), and the label MAP($S/T^3, \chi_2^B, C_s^2$) represents case 2 (with $S/T^3, \chi_2^B$ and $C_s^2$ jointly as evidence), the green curves represents the calculated results of the MAP value in case 1, while the blue curves represents the calculated results of the MAP value in case 2. Subfigures (a)–(j) correspond to the entropy, susceptibility, energy, pressure, trace anomaly, the square of the speed of sound, the specific heat, free energy, the ratio of pressure to the ideal gas limit pressure, and the ratio of the trace anomaly to pressure as functions of temperature, respectively. The lattice results are taken from Refs. [102,103].

lattice simulated smooth crossover reflected by several different thermodynamics. Also obviously we see that the inclusion of $C_s^2$ inside the evidence (case 2) reduces deviations from lattice results on the trace anomaly $[(\epsilon - 3P)/T^4]$ especially in the transition region. These improvements significantly enhance the consistency of the final results with the lattice data, highlight the necessity of including $C_s^2$ within the evidence to refine our Bayesian calibration for the EMD model. We thus adopt case 2 for all subsequent analysis.

### B. Comparison to HRG and HTL

In this subsection, we evaluate both the low and high temperature thermodynamics from our Bayesian holographic model, and confront them (within case 2 analysis) with HRG and HTL estimations. We used the C++ based software package Thermal-FIST [117] to calculate the results of the HRG model. Thermal-FIST is a tool specifically designed for studying heavy-ion collisions and hadronic equations of state. In addition, we incorporated the HTL results [118] for comparison, which provides perturbative estimation over thermodynamics at the high-temperature region.

Figure 6 present posterior results from our model (case 2, blue bands: 95% confidence levels; solid lines: MAP) compared to lattice QCD, HRG, and HTL predictions. In the figures, SB refers to the Stefan Boltzmann limit. We see that at intermediate temperatures (150 MeV $< T <$ 400 MeV), all observables from our model align well with lattice data within uncertainties, with the speed of sound square $C_s^2$ approaching the conformal limit $1/3$ roughly at $T > 300$ MeV. At low temperature regime (100 Mev $< T <$ 150 MeV, the calibrated holographic model aligns with HRG predictions for $\epsilon/T^4, P/T^4$, and $(\epsilon - 3P)/T^4$, while the agreement with lattice data is slightly worse. At high-temperature regime ($T > 400$ MeV), the model results lie well within the uncertainty band of HTL calculations for the trace anomaly $(\epsilon - 3P)/T^4$ and pressure ratio $P/P^{\text{ideal}}$, validating the perturbative asymptotic QCD behavior out of our Bayesian holographic model, though not reaching the SB limit for the chosen temperature range (except for $\chi_2^B$). It is worth noting that the evidence from lattice QCD in the Bayesian inference only cover temperature region 125 MeV $< T <$ 400 MeV. Overall, Fig. 6 indicates that our calibrated holographic model effectively embedded the lattice EoS and generalize well to both low and high temperature with the HRG and HTL predictions automatically matched.

Notably, the specific heat ($C_V$) and free energy ($F$) exhibit single-valued monotonicity, supporting a smooth crossover transition without discontinuities. Minor deviations in $\chi_2^B$ at around 150–250 MeV and its exceeding to the SB limit indicate refinements to the holographic model setup [e.g., $f(\phi)$] could be warranted for future study.

## V. QCD PHASE DIAGRAM IN THE BAYESIAN HOLOGRAPHIC MODEL

In this section, we summarize the posterior distribution of the CEP predicted by the model under the two aforementioned evidence cases based on Bayesian inference, as shown in Fig. 7. The location of the CEP [34,36,37,88,119] is determined by finding the maximum of the gradient of entropy with respect to temperature at zero chemical potential.

Figure 7 displays the CEP locations in the $(T, \mu_B$ plane for both prior (gray) and posterior (red/orange for 95%/68% confidence level) samples, as well as for the MAP (blue triangle). Panel (a) corresponds to case 1 where only $S/T^3$ and $\chi_2^B$ serves as evidence in the Bayesian analysis. The posterior 68% and 95% confidence intervals for the critical temperature and chemical potential are $\mu_B^c$ are $(T^c, \mu_B^c)_{68\%} = (0.0846 - 0.0985, 0.65 - 0.74)$ GeV and $(T^c, \mu_B^c)_{95\%} = (0.0839 - 0.1003, 0.64 - 0.76)$ GeV, respectively, and the MAP result is ($T^c = 0.0909$ GeV, $\mu_B^c = 0.704$ GeV). Panel (b) presents the scenario in which $S/T^3$, $\chi_2^B$ and $C_s^2$ are included in the evidence. The 68% and 95% confidence intervals for $(T^c, \mu_B^c)$ become: $(T^c, \mu_B^c)_{68\%} = (0.0820 - 0.0889, 0.71 - 0.77)$ GeV and $(T^c, \mu_B^c)_{95\%} = (0.0816 - 0.0898, 0.71 - 0.79)$ GeV, respectively, and the MAP result is ($T^c = 0.0859$ GeV, $\mu_B^c = 0.742$ GeV).

Additionally, we compared these results with various other CEP predictions from different theoretical frameworks, such as DSE-FRG [121], FRG [122], the realistic PNJL model [20], and the machine learning method based on EMD [85]. We observed that the machine learning assisted EMD model in previous work [85] falls within the 95% confidence interval of the Bayesian holographic model when $S/T^3$ and $\chi_2^B$ alone are considered evidence [panel (a)]. However, it lies outside the posterior prediction in panel (b), likely because the machine learning analysis did not incorporate $C_s^2$ explicitly as a constraint. Compared to case 1, case 2 incorporates additional the squared speed of sound data as a prior on the basis of case 1. Technically, this leads to differences in the fitting performance of the holographic EMD model to lattice data. Case 2 achieves a better fit to the lattice data. The reason for this difference is that the EMD model we use cannot fully represent the physics of lattice QCD, meaning the accuracy of the fitting cannot be guaranteed, our calculations show that when more constraints are added (case 2: additional inclusion of $C_s^2$ data), the fitting accuracy of the EMD model to lattice data improves (as shown in Fig. 5), however, the predicted location of the CEP depends on the accuracy of the model's fit to the lattice data. Therefore, incorporating the squared

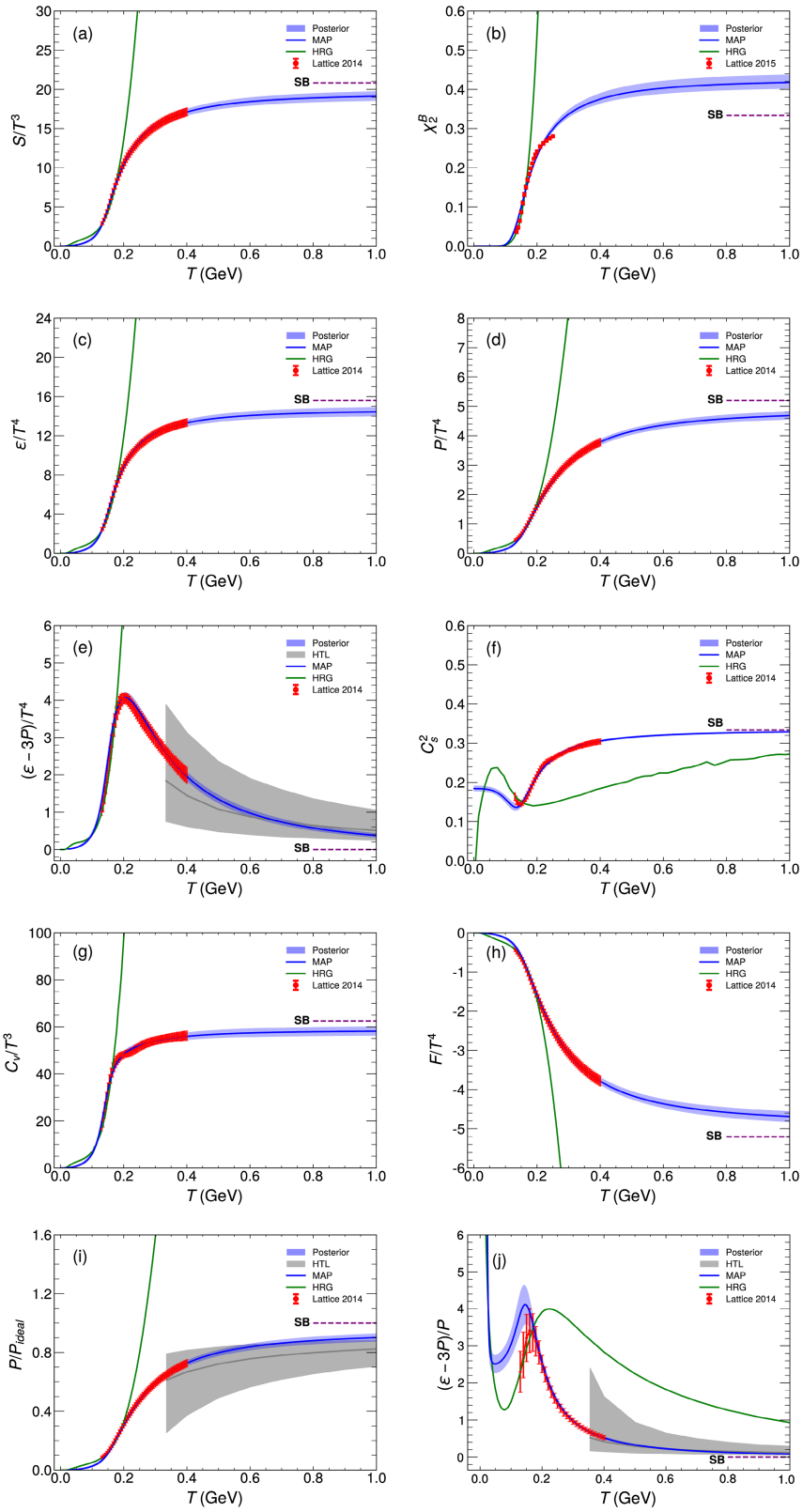



FIG. 6. Calculated the posterior results from our model (case 2, blue bands: 95% confidence levels; solid lines: MAP) compared to lattice QCD, HRG, and HTL predictions. Subfigures (a)–(j) correspond to the entropy, susceptibility, energy, pressure, trace anomaly, the square of the speed of sound, the specific heat, free energy, the ratio of pressure to the ideal gas limit pressure, and the ratio of the trace anomaly to pressure as functions of temperature, respectively. Lattice result from Refs. [102,103], HRG results from Ref. [117], HTL results from Ref. [118].

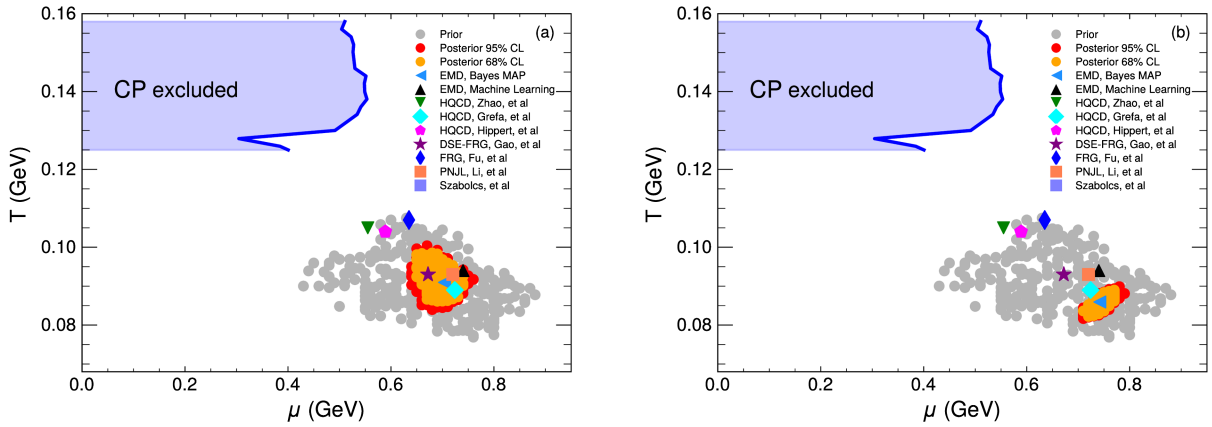



FIG. 7. CEP locations for initial prior samples (gray dots) and posterior samples (red dots at the 95% confidence level and orange dots at the 68% confidence level), The blue triangle indicates MAP result. Panel (a) shows the results obtained when using $S/T^3$ and $\chi_2^B$ as evidence (case 1), while (b) displays those obtained with $S/T^3$, $\chi_2^B$, and $C_s^2$ as evidence (case 2). The black upper triangles are results from the machine learning assisted EMD model [85]. The green lower triangle [120], cyan diamond [44], and magenta pentagon [84] denote predictions from DGR-type holographic QCD models. The purple star, the blue diamond, and the coral square are predictions from DSE-FRG [121], FRG [122] and realistic PNJL model [20], respectively. CEP does not exist in the blue region [123].

speed of sound data has a significant impact on the predicted location of the CEP. Finally, it should be noted that our current calculations and predictions are model dependent. Any modification to the holographic EMD model would consequently alter the Bayesian inference results, posterior calculations, and CEP predictions. The uncertainty in the final results is not only related to the errors in the input lattice data but also to the errors from the Gaussian emulator during the Bayesian inference process. We have considered both factors in our calculations. At the same time, the uncertainty of our holographic EMD model may also affect the final results. The uncertainty in the holographic EMD model arises from the assumed forms of the two functions $f(z)$ (Eq. (18) of the paper) and $A(z)$ (Eq. (24) of the paper). Different assumed forms will lead to minor changes in the final calculation results. We will attempt to address how to incorporate the model's uncertainty into the calculations in our future work.

## VI. CONCLUSION

Building on previous work [69,85], in this paper, we systematically integrate the error estimates from lattice QCD data into a Bayesian holographic model, leveraging Bayesian inference to evaluate the QCD thermodynamics and predict the location of the CEP. In this model, we employ $S/T^3, \chi_2^B$ and $C_s^2$ lattice data as evidence to perform Bayesian inference, yielding a MAP estimate for the CEP at ($T^c = 0.0859$ GeV, $\mu_B^c = 0.742$ GeV). We also provide the corresponding uncertainties for our estimation over the positions of the CEP within both 68% and 95% confidence levels. The 68% and 95% confidence levels for the critical temperature $T^c$ and chemical potential $\mu_B^c$ are $(T^c, \mu_B^c)_{68\%} = (0.0820 - 0.0889, 0.71 - 0.77)$ GeV and $(T^c, \mu_B^c)_{95\%} = (0.0816 - 0.0898, 0.71 - 0.79)$ GeV. Additionally, we used the $C_s^2$ criterion to calculate the temperature range of the smooth crossover at zero chemical potential when $C_s^2$ reaches its minimum in the posterior distribution. The temperature ranges corresponding to the 95% confidence levels is found to be $T_{95\%} =$ 0.1297–0.1386 GeV. Our model's predictions are consistent with results of established theoretical frameworks in their corresponding valid temperature range. From the perspective of CEP predictions, we do have some differences compared to previous predictions. In our calculations, case 2 demonstrates better fitting performance for the lattice data of thermodynamic quantities overall (as shown in Figs. 5–6), and the model's CEP position depends on the fitting performance of the lattice data (as shown in Fig. 7). In the future, we plan to extend our model to calculate additional physical properties for QCD matter, including the in-medium heavy-quark potential [124], diffusion coefficient, and viscosity, to further validate our model's accuracy and applicability.

## ACKNOWLEDGMENTS

This work is supported in part by the National Natural Science Foundation of China (NSFC) Grants No. 12405154, No. 12235016, and No. 12221005 and the Strategic Priority Research Program of Chinese Academy of Sciences under Grant No. XDB34030000, the Fundamental Research Funds for the Central Universities, Open fund for Key Laboratories of the Ministry of Education under Grant No. QLPL2024P01,

CUHK-Shenzhen university development fund under Grant No. UDF01003041 and No. UDF03003041, Shenzhen Peacock fund under No. 2023TC0179, and the European Union—Next Generation EU through the research Grant No. P2022Z4P4B "SOPHYA—Sustainable Optimised PHYsics Algorithms: fundamental physics to build an advanced society" under the program PRIN 2022 PNRR of the Italian Ministero dell'Università e Ricerca (MUR).

## DATA AVAILABILITY

The data that support the findings of this article are openly available [102,103].

[1] K. Adcox *et al.* (PHENIX Collaboration), Formation of dense partonic matter in relativistic nucleus-nucleus collisions at RHIC: Experimental evaluation by the PHENIX collaboration, Nucl. Phys. **A757**, 184 (2005).

[2] M. M. Aggarwal *et al.* (STAR Collaboration), An experimental exploration of the QCD phase diagram: The search for the critical point and the onset of de-confinement, arXiv:1007.2613.

[3] K. Adcox *et al.* (PHENIX Collaboration), Suppression of hadrons with large transverse momentum in central Au + Au collisions at $\sqrt{s_{NN}} = 130$-GeV, Phys. Rev. Lett. **88**, 022301 (2002).

[4] J. Adams *et al.* (STAR Collaboration), Transverse momentum and collision energy dependence of high p(T) hadron suppression in Au + Au collisions at ultrarelativistic energies, Phys. Rev. Lett. **91**, 172302 (2003).

[5] M. Xie, Q.-F. Han, E.-K. Wang, B.-W. Zhang, and H.-Z. Zhang, The medium-temperature dependence of jet transport coefficient in high-energy nucleus–nucleus collisions, Nucl. Sci. Tech. **35**, 125 (2024).

[6] Y. Li, S. Shen, S. Wang, and B.-W. Zhang, Transverse momentum balance of dijets in Xe + Xe collisions at the LHC, Nucl. Sci. Tech. **35**, 113 (2024).

[7] W.-j. Fu, QCD at finite temperature and density within the fRG approach: An overview, Commun. Theor. Phys. **74**, 097304 (2022).

[8] J. N. Guenther, Overview of the QCD phase diagram: Recent progress from the lattice, Eur. Phys. J. A **57**, 136 (2021).

[9] K. Zhou, L. Wang, L.-G. Pang, and S. Shi, Exploring QCD matter in extreme conditions with machine learning, Prog. Part. Nucl. Phys. **135**, 104084 (2024).

[10] L. Du, A. Sorensen, and M. Stephanov, The QCD phase diagram and beam energy scan physics: A theory overview, Int. J. Mod. Phys. E **33**, 2430008 (2024).

[11] X. Luo, S. Shi, N. Xu, and Y. Zhang, A study of the properties of the QCD phase diagram in high-energy nuclear collisions, Particles **3**, 278 (2020).

[12] Y.-G. Ma, L.-G. Pang, R. Wang, and K. Zhou, Phase transition study meets machine learning, Chin. Phys. Lett. **40**, 122101 (2023).

[13] H. Zhang, D. Hou, T. Kojo, and B. Qin, Functional renormalization group study of the quark-meson model with $\omega$ meson, Phys. Rev. D **96**, 114029 (2017).

[14] F. Gao and Y.-x. Liu, QCD phase transitions via a refined truncation of Dyson-Schwinger equations, Phys. Rev. D **94**, 076009 (2016).

[15] S.-x. Qin, L. Chang, H. Chen, Y.-x. Liu, and C. D. Roberts, Phase diagram and critical endpoint for strongly-interacting quarks, Phys. Rev. Lett. **106**, 172301 (2011).

[16] C. Shi, Y.-L. Wang, Y. Jiang, Z.-F. Cui, and H.-S. Zong, Locate QCD critical end point in a continuum model study, J. High Energy Phys. 07 (2014) 014.

[17] A. M. Halasz, A. D. Jackson, R. E. Shrock, M. A. Stephanov, and J. J. M. Verbaarschot, On the phase diagram of QCD, Phys. Rev. D **58**, 096007 (1998).

[18] J. Berges and K. Rajagopal, Color superconductivity and chiral symmetry restoration at nonzero baryon density and temperature, Nucl. Phys. **B538**, 215 (1999).

[19] M. A. Stephanov, QCD phase diagram and the critical point, Prog. Theor. Phys. Suppl. **153**, 139 (2004).

[20] Z. Li, K. Xu, X. Wang, and M. Huang, The kurtosis of net baryon number fluctuations from a realistic Polyakov–Nambu–Jona-Lasinio model along the experimental freeze-out line, Eur. Phys. J. C **79**, 245 (2019).

[21] F. Sun, J. Shao, R. Wen, K. Xu, and M. Huang, Chiral phase transition and spin alignment of vector mesons in the polarized-Polyakov-loop Nambu–Jona-Lasinio model under rotation, Phys. Rev. D **109**, 116017 (2024).

[22] Y.-R. Bao and S.-Q. Feng, Effects of tensor spin polarization on the chiral restoration and deconfinement phase transitions, Phys. Rev. D **109**, 096033 (2024).

[23] J. M. Maldacena, The large N limit of superconformal field theories and supergravity, Adv. Theor. Math. Phys. **2**, 231 (1998).

[24] J. Erdmenger, N. Evans, I. Kirsch, and E. Threlfall, Mesons in gauge/gravity duals—a review, Eur. Phys. J. A **35**, 81 (2008).

[25] S. J. Brodsky, G. F. de Teramond, H. G. Dosch, and J. Erlich, Light-front holographic QCD and emerging confinement, Phys. Rep. **584**, 1 (2015).

[26] J. Casalderrey-Solana, H. Liu, D. Mateos, K. Rajagopal, and U. A. Wiedemann, *Gauge/String Duality, Hot QCD and Heavy Ion Collisions* (Cambridge University Press, Cambridge, England, 2014).

[27] A. Adams, L. D. Carr, T. Schäfer, P. Steinberg, and J. E. Thomas, Strongly correlated quantum fluids: Ultracold quantum gases, quantum chromodynamic plasmas, and holographic duality, New J. Phys. **14**, 115009 (2012).

[28] S.-w. Li and T. Jia, Dynamically flavored description of holographic QCD in the presence of a magnetic field, Phys. Rev. D **96**, 066032 (2017).
[29] K. Bitaghsir Fadafan, F. Kazemian, and A. Schmitt, Towards a holographic quark-hadron continuity, J. High Energy Phys. 03 (2019) 183.
[30] R. Abt, J. Erdmenger, N. Evans, and K. S. Rigatos, Light composite fermions from holography, J. High Energy Phys. 11 (2019) 160.
[31] T. Nakas and K. S. Rigatos, Fermions and baryons as open-string states from brane junctions, J. High Energy Phys. 12 (2020) 157.
[32] D. Li and M. Huang, Dynamical holographic QCD model for glueball and light meson spectra, J. High Energy Phys. 11 (2013) 088.
[33] S. S. Gubser and A. Nellore, Mimicking the QCD equation of state with a dual black hole, Phys. Rev. D **78**, 086007 (2008).
[34] O. DeWolfe, S. S. Gubser, and C. Rosen, A holographic critical point, Phys. Rev. D **83**, 086005 (2011).
[35] M. Jarvinen, Holographic dense QCD in the Veneziano limit, EPJ Web Conf. **274**, 08006 (2022).
[36] Y. Yang and P.-H. Yuan, Confinement-deconfinement phase transition for heavy quarks in a soft wall holographic QCD model, J. High Energy Phys. 12 (2015) 161.
[37] Y. Yang and P.-H. Yuan, A refined holographic QCD model and QCD phase structure, J. High Energy Phys. 11 (2014) 149.
[38] D. Dudal and S. Mahapatra, Thermal entropy of a quark-antiquark pair above and below deconfinement from a dynamical holographic QCD model, Phys. Rev. D **96**, 126010 (2017).
[39] D. Dudal and S. Mahapatra, Interplay between the holographic QCD phase diagram and entanglement entropy, J. High Energy Phys. 07 (2018) 120.
[40] Z. Fang, S. He, and D. Li, Chiral and deconfining phase transitions from holographic QCD study, Nucl. Phys. **B907**, 187 (2016).
[41] X.-Y. Liu, X.-C. Peng, Y.-L. Wu, and Z. Fang, Holographic study on QCD phase transition and phase diagram with two flavors, Phys. Rev. D **109**, 054032 (2024).
[42] Y.-Y. Li, X.-L. Liu, X.-Y. Liu, and Z. Fang, Correlations between the deconfining and chiral transitions in holographic QCD, Phys. Rev. D **105**, 034019 (2022).
[43] R. Critelli, J. Noronha, J. Noronha-Hostler, I. Portillo, C. Ratti, and R. Rougemont, Critical point in the phase diagram of primordial quark-gluon matter from black hole physics, Phys. Rev. D **96**, 096026 (2017).
[44] J. Grefa, J. Noronha, J. Noronha-Hostler, I. Portillo, C. Ratti, and R. Rougemont, Hot and dense quark-gluon plasma thermodynamics from holographic black holes, Phys. Rev. D **104**, 034002 (2021).
[45] I. Y. Aref'eva, A. Ermakov, and P. Slepov, Direct photons emission rate and electric conductivity in twice anisotropic QGP holographic model with first-order phase transition, Eur. Phys. J. C **82**, 85 (2022).
[46] I. Y. Aref'eva, K. Rannu, and P. Slepov, Holographic model for heavy quarks in anisotropic hot dense QGP with external magnetic field, J. High Energy Phys. 07 (2021) 161.
[47] X. Chen, D. Li, and M. Huang, Criticality of QCD in a holographic QCD model with critical end point, Chin. Phys. C **43**, 023105 (2019).
[48] X. Chen, S.-Q. Feng, Y.-F. Shi, and Y. Zhong, Moving heavy quarkonium entropy, effective string tension, and the QCD phase diagram, Phys. Rev. D **97**, 066015 (2018).
[49] X. Chen, L. Zhang, D. Li, D. Hou, and M. Huang, Gluodynamics and deconfinement phase transition under rotation from holography, J. High Energy Phys. 07 (2021) 132.
[50] J. Zhou, X. Chen, Y.-Q. Zhao, and J. Ping, Thermodynamics of heavy quarkonium in a magnetic field background, Phys. Rev. D **102**, 086020 (2020).
[51] X. Chen, D. Li, D. Hou, and M. Huang, Quarkyonic phase from quenched dynamical holographic QCD model, J. High Energy Phys. 03 (2020) 073.
[52] X. Cao, M. Baggioli, H. Liu, and D. Li, Pion dynamics in a soft-wall AdS-QCD model, J. High Energy Phys. 12 (2022) 113.
[53] M. Arcos, W. Fischler, J. F. Pedraza, and A. Svesko, Membrane nucleation rates from holography, J. High Energy Phys. 12 (2022) 141.
[54] X. Cao and H. Liu, The impact of the phase transition on quark-gluon plasma with an extremely strong magnetic field in holographic QCD, Phys. Rev. D **111**, 026008 (2025).
[55] H. Bohra, D. Dudal, A. Hajilou, and S. Mahapatra, Chiral transition in the probe approximation from an Einstein-Maxwell-dilaton gravity model, Phys. Rev. D **103**, 086021 (2021).
[56] I. Y. Aref'eva, A. Hajilou, K. Rannu, and P. Slepov, Magnetic catalysis in holographic model with two types of anisotropy for heavy quarks, Eur. Phys. J. C **83**, 1143 (2023).
[57] H. Bohra, D. Dudal, A. Hajilou, and S. Mahapatra, Anisotropic string tensions and inversely magnetic catalyzed deconfinement from a dynamical AdS/QCD model, Phys. Lett. B **801**, 135184 (2020).
[58] K. Hashimoto, S. Sugishita, A. Tanaka, and A. Tomiya, Deep learning and the AdS/CFT correspondence, Phys. Rev. D **98**, 046019 (2018).
[59] K. Hashimoto, S. Sugishita, A. Tanaka, and A. Tomiya, Deep learning and holographic QCD, Phys. Rev. D **98**, 106014 (2018).
[60] T. Akutagawa, K. Hashimoto, and T. Sumimoto, Deep learning and AdS/QCD, Phys. Rev. D **102**, 026020 (2020).
[61] K. Hashimoto, K. Ohashi, and T. Sumimoto, Deriving the dilaton potential in improved holographic QCD from the chiral condensate, Prog. Theor. Exp. Phys. **2023**, 033B01 (2023).
[62] Y.-K. Yan, S.-F. Wu, X.-H. Ge, and Y. Tian, Deep learning black hole metrics from shear viscosity, Phys. Rev. D **102**, 101902 (2020).
[63] M. Song, M. S. H. Oh, Y. Ahn, and K.-Y. Kima, AdS/deep-learning made easy: Simple examples, Chin. Phys. C **45**, 073111 (2021).
[64] W.-B. Chang and D.-f. Hou, Heavy quarkonium spectral function in an anisotropic background, Phys. Rev. D **109**, 086010 (2024).

[65] B. Ahn, H.-S. Jeong, K.-Y. Kim, and K. Yun, Deep learning bulk spacetime from boundary optical conductivity, J. High Energy Phys. 03 (2024) 141.
[66] Z.-F. Gu, Y.-K. Yan, and S.-F. Wu, Neural ODEs for holographic transport models without translation symmetry, Eur. Phys. J. C **85**, 63 (2025).
[67] K. Li, Y. Ling, P. Liu, and M.-H. Wu, Learning the black hole metric from holographic conductivity, Phys. Rev. D **107**, 066021 (2023).
[68] B. Ahn, H.-S. Jeong, K.-Y. Kim, and K. Yun, Holographic reconstruction of black hole spacetime: Machine learning and entanglement entropy, J. High Energy Phys. 01 (2025) 025.
[69] X. Chen and M. Huang, Machine learning holographic black hole from lattice QCD equation of state, Phys. Rev. D **109**, L051902 (2024).
[70] Y. Chen, X. Chen, D. Li, and M. Huang, Deconfinement and chiral restoration phase transition under rotation from holography in an anisotropic gravitational background, Phys. Rev. D **111**, 046006 (2025).
[71] M. Xie, W. Ke, H. Zhang, and X.-N. Wang, Global constraint on the jet transport coefficient from single-hadron, dihadron, and $\gamma$-hadron spectra in high-energy heavy-ion collisions, Phys. Rev. C **109**, 064917 (2024).
[72] W.-J. Xing, S. Cao, and G.-Y. Qin, Flavor hierarchy of parton energy loss in quark-gluon plasma from a Bayesian analysis, Phys. Lett. B **850**, 138523 (2024).
[73] J. Wu, W. Ke, and X.-N. Wang, Bayesian inference of the path-length dependence of jet energy loss, Phys. Rev. C **108**, 034911 (2023).
[74] L. Zhu, Z. Gao, W. Ke, and H. Zhang, Bayesian inference of the magnetic field and chemical potential on holographic jet quenching in heavy-ion collisions, arXiv:2506.00340.
[75] W. Fan *et al.* (JETSCAPE Collaboration), New metric improving Bayesian calibration of a multistage approach studying hadron and inclusive jet suppression, Phys. Rev. C **109**, 064903 (2024).
[76] Y. He, L.-G. Pang, and X.-N. Wang, Bayesian extraction of jet energy loss distributions in heavy-ion collisions, Phys. Rev. Lett. **122**, 252302 (2019).
[77] J. Mulligan *et al.* (JETSCAPE Collaboration), Determining the jet transport coefficient $\hat{q}$ of the quark-gluon plasma using Bayesian parameter estimation, in 55th Rencontres de Moriond on QCD and High Energy Interactions (2021), arXiv:2106.11348.
[78] J. E. Parkkila, A. Onnerstad, and D. J. Kim, Bayesian estimation of the specific shear and bulk viscosity of the quark-gluon plasma with additional flow harmonic observables, Phys. Rev. C **104**, 054904 (2021).
[79] J. E. Bernhard, J. S. Moreland, and S. A. Bass, Bayesian estimation of the specific shear and bulk viscosity of quark–gluon plasma, Nat. Phys. **15**, 1113 (2019).
[80] Y.-L. Cheng, S. Shi, Y.-G. Ma, H. Stöcker, and K. Zhou, Examination of nucleon distribution with Bayesian imaging for isobar collisions, Phys. Rev. C **107**, 064909 (2023).
[81] S. Pratt, E. Sangaline, P. Sorensen, and H. Wang, Constraining the equation of state of super-hadronic matter from heavy-ion collisions, Phys. Rev. Lett. **114**, 202301 (2015).
[82] J. E. Bernhard, J. S. Moreland, S. A. Bass, J. Liu, and U. Heinz, Applying Bayesian parameter estimation to relativistic heavy-ion collisions: Simultaneous characterization of the initial state and quark-gluon plasma medium, Phys. Rev. C **94**, 024907 (2016).
[83] Y.-L. Du, K. Zhou, J. Steinheimer, L.-G. Pang, A. Motornenko, H.-S. Zong, X.-N. Wang, and H. Stöcker, Identifying the nature of the QCD transition in relativistic collision of heavy nuclei with deep learning, Eur. Phys. J. C **80**, 516 (2020).
[84] M. Hippert, J. Grefa, T. A. Manning, J. Noronha, J. Noronha-Hostler, I. Portillo Vazquez, C. Ratti, R. Rougemont, and M. Trujillo, Bayesian location of the QCD critical point from a holographic perspective, Phys. Rev. D **110**, 094006 (2024).
[85] X. Chen and M. Huang, Flavor dependent critical endpoint from holographic QCD through machine learning, J. High Energy Phys. 02 (2025) 123.
[86] D. Li, S. He, M. Huang, and Q.-S. Yan, Thermodynamics of deformed $AdS_5$ model with a positive/negative quadratic correction in graviton-dilaton system, J. High Energy Phys. 09 (2011) 041.
[87] R.-G. Cai, S. He, and D. Li, A hQCD model and its phase diagram in Einstein-Maxwell-Dilaton system, J. High Energy Phys. 03 (2012) 033.
[88] S. He, S.-Y. Wu, Y. Yang, and P.-H. Yuan, Phase structure in a dynamical soft-wall holographic QCD model, J. High Energy Phys. 04 (2013) 093.
[89] S. Lin, X. Liu, X. Chen, Z. Gen-Fa, and J. Zhou, Holographic Schwinger effect in flavor-dependent systems, Phys. Rev. D **111**, 046005 (2025).
[90] L. Zhang and M. Huang, Holographic cold dense matter constrained by neutron stars, Phys. Rev. D **106**, 096028 (2022).
[91] B. Chen, X. Chen, X. Li, Z.-R. Zhu, and K. Zhou, Exploring transport properties of quark-gluon plasma with a machine-learning assisted holographic approach, Phys. Rev. D **111**, 086033 (2025).
[92] M. Natsuume, AdS/CFT duality user guide, Lect. Notes Phys. **903**, 1 (2015).
[93] M.-W. Li, Y. Yang, and P.-H. Yuan, Analytic study on chiral phase transition in holographic QCD, J. High Energy Phys. 02 (2021) 055.
[94] Y. Yang and P.-H. Yuan, Universal behaviors of speed of sound from holography, Phys. Rev. D **97**, 126009 (2018).
[95] U. Gursoy, M. Jarvinen, and G. Nijs, Holographic QCD in the Veneziano limit at a finite magnetic field and chemical potential, Phys. Rev. Lett. **120**, 242002 (2018).
[96] J. Novak, K. Novak, S. Pratt, J. Vredevoogd, C. Coleman-Smith, and R. Wolpert, Determining fundamental properties of matter created in ultrarelativistic heavy-ion collisions, Phys. Rev. C **89**, 034917 (2014).
[97] E. Sangaline and S. Pratt, Toward a deeper understanding of how experiments constrain the underlying physics of heavy-ion collisions, Phys. Rev. C **93**, 024908 (2016).
[98] J. E. Bernhard, P. W. Marcy, C. E. Coleman-Smith, S. Huzurbazar, R. L. Wolpert, and S. A. Bass, Quantifying properties of hot and dense QCD matter through

systematic model-to-data comparison, Phys. Rev. C **91**, 054910 (2015).
[99] M. Xie, W. Ke, H. Zhang, and X.-N. Wang, Information-field-based global Bayesian inference of the jet transport coefficient, Phys. Rev. C **108**, L011901 (2023).
[100] S. Cao *et al.* (JETSCAPE Collaboration), Determining the jet transport coefficient qhat from inclusive hadron suppression measurements using Bayesian parameter estimation, Phys. Rev. C **104**, 024905 (2021).
[101] M. Omana Kuttan, J. Steinheimer, K. Zhou, and H. Stoecker, QCD equation of state of dense nuclear matter from a Bayesian analysis of heavy-ion collision data, Phys. Rev. Lett. **131**, 202303 (2023).
[102] A. Bazavov *et al.* (HotQCD Collaboration), Equation of state in $(2+1)$-flavor QCD, Phys. Rev. D **90**, 094503 (2014).
[103] A. Bazavov *et al.*, The QCD equation of state to $\mathcal{O}(\mu_B^6)$ from lattice QCD, Phys. Rev. D **95**, 054504 (2017).
[104] D. Foreman-Mackey, D. W. Hogg, D. Lang, and J. Goodman, EMCEE: The MCMC hammer, Publ. Astron. Soc. Pac. **125**, 306 (2013).
[105] J. Goodman and J. Weare, Ensemble samplers with affine invariance, Commun. Appl. Math. Comput. Sci. **5**, 65 (2010).
[106] B. Tang, Orthogonal array-based latin hypercubes, J. Am. Stat. Assoc. **88**, 1392 (1993).
[107] M. D. Morris and T. J. Mitchell, Exploratory designs for computational experiments, J. Stat. Plann. Infer. **43**, 381 (1995).
[108] J. Loeppky, J. Sacks, and W. Welch, Choosing the sample size of a computer experiment: A practical guide, Technometrics **51**, 366 (2009).
[109] M. E. Tipping and C. M. Bishop, Mixtures of probabilistic principal component analyzers, Neural Comput. **11**, 443 (1999).
[110] C. K. Williams and C. E. Rasmussen, *Gaussian Processes for Machine Learning* (MIT Press Cambridge, MA, 2006), Vol. 2.
[111] L.-G. Pang, K. Zhou, N. Su, H. Petersen, H. Stöcker, and X.-N. Wang, An equation-of-state-meter of quantum chromodynamics transition from deep learning, Nat. Commun. **9**, 210 (2018).
[112] M. Omana Kuttan, K. Zhou, J. Steinheimer, A. Redelbach, and H. Stoecker, An equation-of-state-meter for CBM using PointNet, J. High Energy Phys. 10 (2020) 184.
[113] L. Jiang, L. Wang, and K. Zhou, Deep learning stochastic processes with QCD phase transition, Phys. Rev. D **103**, 116023 (2021).
[114] G. Aarts, K. Fukushima, T. Hatsuda, A. Ipp, S. Shi, L. Wang, and K. Zhou, Physics-driven learning for inverse problems in quantum chromodynamics, Nat. Rev. Phys. **7**, 154 (2025).
[115] N. Metropolis, A. W. Rosenbluth, M. N. Rosenbluth, A. H. Teller, and E. Teller, Equation of state calculations by fast computing machines, J. Chem. Phys. **21**, 1087 (1953).
[116] W. K. Hastings, Monte Carlo sampling methods using Markov chains and their applications, Biometrika **57**, 97 (1970).
[117] V. Vovchenko and H. Stoecker, Thermal-FIST: A package for heavy-ion collisions and hadronic equation of state, Comput. Phys. Commun. **244**, 295 (2019).
[118] N. Haque, A. Bandyopadhyay, J. O. Andersen, M. G. Mustafa, M. Strickland, and N. Su, Three-loop HTLpt thermodynamics at finite temperature and chemical potential, J. High Energy Phys. 05 (2014) 027.
[119] R.-G. Cai, S. He, L. Li, and Y.-X. Wang, Probing QCD critical point and induced gravitational wave by black hole physics, Phys. Rev. D **106**, L121902 (2022).
[120] Y.-Q. Zhao, S. He, D. Hou, L. Li, and Z. Li, Phase diagram of holographic thermal dense QCD matter with rotation, J. High Energy Phys. 04 (2023) 115.
[121] F. Gao and J. M. Pawlowski, QCD phase structure from functional methods, Phys. Rev. D **102**, 034027 (2020).
[122] W.-j. Fu, J. M. Pawlowski, and F. Rennecke, QCD phase structure at finite temperature and density, Phys. Rev. D **101**, 054032 (2020).
[123] S. Borsanyi, Z. Fodor, J. N. Guenther, P. Parotto, A. Pasztor, C. Ratti, V. Vovchenko, and C. H. Wong, Lattice QCD constraints on the critical point from an improved precision equation of state, arXiv:2502.10267.
[124] O.-Y. Luo, X. Chen, F.-P. Li, X.-H. Li, and K. Zhou, Neural network modeling of heavy-quark potential from holography, Eur. Phys. J. C **85**, 637 (2025).